The effects of field line curvature (FLC) scattering on ring current dynamics and ionospheric electrodynamics

Yiqun Yu[1,2], Xingbin Tian[1], Vania Jordanova[3]

[1]School of Space and Environment, Beihang University, Beijing, China

[2]Key Laboratory of Space Environment Monitoring and Information Processing, Ministry of Industry and Information Technology, Beijing, China

[3]Space Science and Application, Los Alamos National Laboratory, Los Alamos, NM, USA

Key Points:

- Ion precipitation associated with FLC scattering is confined outside L=5; additional scattering process is needed in the inner zone
- This process contributes significantly to the ring current decay; it can explain the formation of isotropic boundary
- The precipitating energy flux of protons due to FLC scattering is sometime comparable to that of electrons on the nightside

Corresponding author: Yiqun Yu, yiqunyu17@gmail.com

Abstract

In the ring current dynamics, various loss mechanisms contribute to the ring current decay, including the loss to the upper atmosphere through particle precipitation. This study implements the field-line curvature (FLC) scattering mechanism in a kinetic ring current model and investigates its role in precipitating ions into the ionosphere. The newly included process is solved via a diffusion equation in the model with associated pitch-angle dependent diffusion coefficients. The simulation results indicate that (1) the FLC scattering process exert mostly on energetic ions above 30 keV on the nightside where the magnetospheric configuration is more stretching. Such ion loss thereafter leads to a faster recovery of the ring current. (2) The FLC-associated ion precipitation mainly occurs in the outer region (L>5 for protons and L>4.5 for oxygen ions) on the nightside, and the oxygen ion precipitation takes places in a wider region than protons although its intensity is much lower. Comparisons with POES observations suggest that more precipitation is needed in the inner region, implying that other loss process is required in the model. (3) We further found that the precipitating energy flux of protons due to the FLC scattering can sometimes become comparable to the one from the electrons on the nightside, although electrons usually dominate the ionospheric energy deposit from the midnight eastward towards the dayside. (4) Finally, the FLC scattering process seems to be capable of explaining the formation of the isotropic boundary in the ionosphere.

1 Introduction

It is generally understood that the Earth ring current is composed of both electron and ion species, mainly H^+, He^+, and O^+. The energy content of the ring current during storm time is dominantly from these ion species. Therefore ion loss processes can influence the intensity of the ring current while competing with energization processes. Ions can be supplied from the tail plasma sheet into the inner magnetosphere by convective electric field, gaining energies adiabatically. They move westward around the Earth due to magnetic gradient and curvature effects. Along their pathways, the ring current ions can be lost via charge exchange with neutral hydrogen when they encounter the geocorona [*Dessler and Parker*, 1959] and become neutralized. They can also lose energy and be scattered by the plasmaspheric ions and electrons due to Coulomb collision when they move through the ambient thermal plasma [*Jordanova et al.*, 1996].

Of importance for the ring current decay are two additional collisionless scattering mechanisms, which may have significant impact on the ring current dynamics: wave-particle interactions and field line curvature (FLC) scattering. Electromagnetic ion cyclotron (EMIC) waves can resonate with energetic ring current ions once the wave frequency satisfies the resonate condition. While this process depends on the wave intensity and location, the FLC scattering is controlled by the geometry of magnetic field lines and occurs where the field line curvature radius is comparable to the gyroradius of particles [*Tsyganenko*, 1982; *Delcourt et al.*, 1996; *Serggev et al.*, 1983], thus resulting in chaotic motion of the particles. Due to the much smaller gyroradius of electrons, the FLC scattering loss is more efficient on ions. Stretched magnetic field lines possess smaller curvature radius and therefore are more applicable for FLC scattering. Such condition often appears near the equatorial current sheet on the nightside, and FLC scattering is also named as current sheet scattering. Both collisionless mechanisms play the role of scattering ring current ions and changing particle distributions. *Ebihara et al.* [2011] examined the decay of ring current due to FLC scattering and found that the ring current shows rapid recovery with a e-folding time of 6 hour when the FLC scattering is included, as opposed to a e-folding time of 12 hour when it is excluded. Their study assumed that the FLC scattering works on protons only while its impact on other ion species was not considered. However it is known that the oxygen ions could sometime exceed the number density of protons and are of the same importance to the ring current growth during geomagnetic disturbed time [*Fernandes et al.*, 2017; *Yue et al.*, 2019] and that the oxygen ion is more effectively influenced by the FLC scattering because of its larger gyroradius, therefore the contribution of O^+ precipitation may not be negligible. The study of *Ebihara et al.* [2011] thus provided a lower limit of the rapid decay of the ring current due to FLC scattering mechanism.

Besides the impact on the ring current dynamics, the FLC scattering process is believed to be associated with the formation of isotropic boundary (IB) [*Sergeev et al.*, 1993; *Sergeev and Gvozdevsky*, 1995; *Meurant et al.*, 2007], a region in the auroral zone where the precipitating flux changes abruptly. Equatorward of the IB, the trapped particle flux is much higher than the precipitating flux, while the two are comparable poleward of the IB. In other words, the loss cones are filled up at higher latitudes whereas they are empty at lower latitudes of the IB. This boundary is identified in many observations as the low-Earth-orbit satellites (e.g., DMSP, NOAA/POES) travel across

it [*Newell et al.*, 1998; *Dubyagin et al.*, 2018]. Such a boundary characterizes a transition from weak precipitation to strong isotropic precipitation at higher latitudes and maps to the magnetosphere location across which the rate of pitch angle scattering varies greatly. While EMIC waves are suggested to play a part, mostly at lower latitudes and local-time dependent, studies show that the FLC scattering may act as the major process for the IB formation [*Ganushkina et al.*, 2005; *Haiducek et al.*, 2018; *Yue et al.*, 2014; *Dubyagin et al.*, 2018].

Resulting from the ring current ion scattering loss, proton precipitation is produced into the upper atmosphere, which subsequently generates proton auroras. They are typically observed in two spatial regions [*Sraas et al.*, 1977], with one at high latitudes, corresponding to proton auroral oval, and the other one at subauroral region, separated from the high-latitude electron and proton auroral ovals. The latter often appears as spots or bands extended longitudinally. Previous studies have found close association between subauroral proton precipitation with EMIC waves in different locations (see review by [*Frey*, 2007; *Yahnin and Yahnina*, 2007]), such as dayside proton flashes [*Fuselier et al.*, 2004; *Hubert et al.*, 2003] and afternoon/nightside detached proton arcs [e.g., *Immel et al.*, 2002; *Spasojevic et al.*, 2004; *Spasojevic and Fuselier*, 2009; *Jordanova et al.*, 2007; *Nishimura et al.*, 2014]. The EMIC wave-driven proton precipitation could occur in localized regions where the local plasma conditions meet instability threshold and excite EMIC waves [e.g., *Jordanova et al.*, 1997]. Such locations can be spotty or elongated, as inferred from the auroral images. On the other hand, the FLC scattering-driven proton precipitation may take place over a much wider region if the nightside magnetic field lines are sufficiently stretched in a global scale. With the proton precipitation, one can monitor the degree of magnetic field stretching in the magnetotail and further help understand the magnetic mapping. *Liang et al.* [2013] proposed a technique to derive the magnetic field line curvature with in-situ measurements and evaluate the proton precipitation fluxes to estimate the MI mapping. Their study excluded the effects of EMIC waves on the precipitation by selecting events without EMIC activities. While it is highly possible that the proton precipitation led by EMIC-proton interactions and that due to FLC scattering coexists, the assessment on the role of both mechanisms is required in order to achieve better understanding of the proton auroral dynamics. However, compared to extensive studies on the association of proton aurora precipitation with EMIC waves [e.g., *Jordanova et al.*, 2007; *Nishimura et al.*, 2014;

Yahnina and Yahnin, 2014; *Yahnin and Yahnina*, 2007; *Spasojevic and Fuselier*, 2009; *Spasojevic et al.*, 2004; *Fuselier et al.*, 2004; *Chen et al.*, 2014], the investigation on the association with the FLC scattering is still lacking.

Recently, *Chen et al.* [2019] included the FLC scattering mechanism in their RCM-E ring current model and compared the electron and ion precipitating flux and their respective effects on the ionospheric electrodynamics. They found that the FLC-associated ion scattering contributes much less to the precipitating energy flux and thus the resultant conductance of the ion diffuse aurora is far smaller than that of electron aurora. They used a simplified model for the FLC scattering loss rate, independent on pitch angles. In this study, we will also investigate the effect of FLC scattering on the ionospheric ion precipitation, as well as on the ring current decay. However, unlike *Chen et al.* [2019], we implement the FLC scattering mechanism in the ring current model as a diffusion process by solving related diffusion coefficients that are energy and pitch angle dependent. We simulate the March 17, 2013 storm event to understand the role of FLC scattering in changing the ring current dynamics, the global pattern of diffuse aurora, and the IB positions. Section 2 describes the model and the newly implemented FLC scattering loss mechanism. Setion 3 presents simulation results on the morphology of ion precipitation associated with the FLC scattering, the subsequent effects on the ring current decay and ionospheric precipitation, as well as the relationship with the IB. Section 4 summarizes this study.

2 Model description

The kinetic ring current model used to study the role of FLC scattering is the ring current-atmosphere interactions model (RAM) coupled with a self-consistent (SC) magnetic field (B) and electric field code [*Jordanova et al.*, 2006; *Zaharia et al.*, 2006; *Yu et al.*, 2017]. This RAM-SCB model mainly solves the bounce-averaged Fokker-Planck equation of distribution functions $F_l(t)$ for three ring current ion species (H^+, He^+,O^+) and electrons:

$$\frac{\partial F_l(t,R,\phi,E,\alpha)}{\partial t}+\frac{1}{R_o^2}\frac{\partial}{\partial R_o}(R_o^2<\frac{dR_o}{dt}>F_l)+\frac{\partial}{\partial\phi}(<\frac{d\phi}{dt}>F_l)$$
$$+\frac{1}{\gamma p}\frac{\partial}{\partial E}(\gamma p<\frac{dE}{dt}>F_l)+\frac{1}{h\mu_o}\frac{\partial}{\partial\mu_o}(h\mu_o<\frac{d\mu_o}{dt}>F_l)$$

$$=< (\frac{\partial F_l}{\partial t})_{loss} > \tag{1}$$

where the distribution function F_l is solved in the magnetic equatorial plane within a radial distance of 2.0<R<6.5 R_e, covering all magnetic local times ϕ, pitch angles α ($\mu = \cos\alpha$, α from 0 to 90°), and kinetic energy E from 0.15 to 400 keV. The subscription l represents particle species, the bracket <> denotes the bounce-average effect, the subscription o indicates the equatorial plane, p is the relativistic momentum of the particle, γ is the Lorentz factor, and h, which is proportional to the bounce period along magnetic field lines, is defined by:

$$h(\mu_o) = \frac{1}{2R_0} \int_{s_m}^{s_m'} \frac{ds}{\sqrt{(1 - B(s)/B_m)}} \tag{2}$$

Here, B_m is the magnetic field at the mirror point, ds is a distance interval along the field line, and R_0 is the distance between the Earth center and the intersection of the field line with the equatorial plane.

The time-dependent conditions that drive the variations of the above distribution function mainly lie in the following three aspects: (1) the outer boundary conditions at 6.5 R_e, (2) the electric field condition, and (3) the magnetic field condition. The outer boundary condition, assumed isotropic, is obtained from the Los Alamos geosynchronous spacecraft that measure particle fluxes at various energy channels. The measured ion fluxes are decoupled into different ion species according to their statistical fractions derived by *Young et al.* [1982]. These fractions vary as a function of Kp index. The electric field or the electric potential is self-consistently estimated within the ring current model [*Yu et al.*, 2017]. Note that the inductive electric field is not included in this study. Mapped to the equatorial plane, the ionospheric electric potential is determined by field-aligned currents (FACs) and ionospheric conductance. The FACs, mainly Region-2 type, are diverted from the partial ring current [*Vasyliunas*, 1970] in the equator. The ionospheric conductance is originated from two energy sources: the solar radiation and electron precipitation. The solar radiation induced conductance can be estimated based on empirical functions with solar zenith angle and F10.7 index [*Moen and Brekke*, 1993]. The electron precipitation associated conductance is determined by Robinson formula [*Robinson et al.*, 1987] that relates the conductance to the energy flux and

averaged energy of precipitating electrons that are diffused into loss cone from the ring current. As for the magnetic field condition, the ring current model is coupled self-consistently to a 3-D equilibrium code that computes the magnetic field from the anisotropic plasma conditions [*Zaharia et al.*, 2004, 2006]. With the supply of plasma source from the boundary, mostly on the nightside, the above electric and magnetic field drive the particles to move toward and around the Earth, violating the third adiabatic invariant if the global change of the magnetic field configuration is on the order of drift period of particles, thus leading to their energization and the increase of ring current intensity.

The loss processes that decay the ring current stem from both ions and electrons. Although electrons contribution is minor to the ring current energy content as opposed to ions, it is found to be not negligible as electrons could contribute as much as 20% in storms [*Jordanova et al.*, 2012]. In addition to being depleted at the dayside magnetopause boundary, the loss of electrons are partly caused by scattering into their loss cones and precipitating into the upper atmosphere. Such scattering process is mostly a result of cyclotron wave-particle interactions when the electrons gyrorate at a frequency Ω_c that satisfies the resonant condition. Gyroresonant interactions with waves can lead particles to diffuse in pitch angle. The responsible waves included in this ring current model are whistler-mode waves, such as chorus waves outside plasmapause and hiss waves inside plasmapause [e.g., *Ni et al.*, 2016]. In this study, the electrostatic electron cyclotron harmonic (ECH) wave is not included.

The electron scattering process, or diffusion, can be accounted for via the diffusion equation:

$$< (\frac{\partial F_l}{\partial t}) >= \frac{1}{h\mu_o}\frac{\partial}{\partial \mu_o}\left[h\mu_o < D_{\mu_o\mu_o} > \frac{\partial F_l}{\partial \mu_o}\right]$$
$$< D_{\mu_o\mu_o} >= (1-\mu_o^2) < D_{\alpha\alpha} > \quad (3)$$

where $< D_{\alpha\alpha} > (E, \alpha)$ is bounce-averaged pitch angle diffusion coefficients associated with wave-particle resonant interactions. The coefficients associated with chorus waves are determined from quasi-linear theory using the PADIE code [*Glauert and Horne*, 2005; *Horne et al.*, 2013; *Glauert et al.*, 2014], based on statistical observations of wave properties for regions outside the plasmapause. The coefficients associated with hiss waves are computed from a similar code by *Albert* [2005]. The

electrons diffused into their loss cones then participate in changing the auroral conductance, as a major energy source to the ionosphere.

For ions, their loss processes in the model include charge exchange with geocoronal hydrogens, drift out of the magnetopause boundary, atmospheric collisional loss, and collisionless pitch angle diffusion into loss cones for precipitation. The collisionless scattering mechanism newly implemented in the model is the FLC scattering, which is solved via the same diffusion equation in Eqn. (3). The diffusion coefficients $D_{\alpha\alpha}$ are computed based on the geometry of magnetic field lines, previously formulated by *Young et al.* [2008]:

$$
\begin{aligned}
D_{\alpha\alpha} &= D\frac{N^2\sin^2(\omega(\varepsilon)\alpha_0)\cos^{2b(\varepsilon)}(\alpha_0)}{\sin^2(\alpha_0)\cos^2(\alpha_0)} \\
D &= \frac{A^2_{max}(\varepsilon,\eta_1,\eta_2)}{2\tau_B} \\
N &= [\sin(\omega(\varepsilon)\alpha_0)\cos^{b(\varepsilon)}(\alpha_0)]^{-1}|_{\alpha_0=\overline{\alpha_0}} \\
A_{max} &= exp(c(\varepsilon))(\eta_1^{a1(\varepsilon)}\eta_2^{a2(\varepsilon)} + d(\varepsilon))
\end{aligned}
\tag{4}
$$

Here $\varepsilon = R_G/R_C$ is a parameter representing the degree of chaotic scattering due to FLC effects. R_G is the particle gyroradius in the equatorial plane, and R_C is the field line curvature radius:

$$
\frac{1}{\overrightarrow{R}_c} = (\overrightarrow{b}\cdot\nabla)\overrightarrow{b} \tag{5}
$$

where $\overrightarrow{b}$ is the unit vector of magnetic field at the magnetic equator $\overrightarrow{b} = \overrightarrow{B}/B$. The critical threshold of ε is chosen at 0.1 in this study, below which the chaotic scattering is considered weak and the diffusion coefficient is not calculated. This is equivalent to the theoretical adiabaticity parameter K, the reversal of ε. Typically, a value of $K = 8$ marks the transition from a weakly scattering condition to a strongly scattering condition ([*Sergeev et al.*, 1983]) and is applied in many studies for studying the IB location. [e.g., *Liang et al.*, 2013; *Yue et al.*, 2014; *Gilson et al.*, 2012]. But this theoretical value has recently been challenged because researchers found that this scattering threshold could be much higher or within a certain range [*Ilie et al.*, 2015; *Dubyagin et al.*, 2018; *Haiducek et al.*, 2018]. Recent study of *Haiducek et al.* [2018] used multiple magnetospheric models to determine the accuracy of K estimation and reported constraints on the range of K values, which

subsequently is found to be close to the above theoretical threshold. *Dubyagin et al.* [2018] also reported statistical distribution of the estimated K parameter to be around 9-13. Therefore, in this study, we adopt the ε value of 0.1 as the transition threshold, close to the reversal of $K = 10$.

In the above equation, $\eta_1 = R_C(\delta^2 R_C/\delta s^2)$ and $\eta_2 = R_C^2/B_0(\delta^2 B_0/\delta s^2)$ are measures of the changing curvature radius R_C and magnetic field B_0 in the equatorial plane, respectively (s is the distance along the field line away from the equator). τ_B is the bounce period between two magnetic mirror points, equivalent with the h parameter in Eqn. (2). $\overline{\alpha_0}$ is the equatorial pitch angle, at which the angle-dependent quantity $\sin(\omega\alpha_0)\cos^b(\varepsilon)(\alpha_0)$ reaches its maximum. [*Young et al.*, 2002]. Parameters of $a1(\varepsilon), a2(\varepsilon), c(\varepsilon)$, and $d(\varepsilon)$ are determined in the form of $q = \sum_{n=0}^{N} q_n \varepsilon^{-n}$ with the coefficients q_n listed in Table 2 of *Young et al.* [2002].

From the above formula, it is evident that $D_{\alpha\alpha}$ is controlled by the parameter of ε, which depends on not only the geometry of the in-situ magnetic field lines, but also the gyroradius, or the mass of particles. So as the ring current electrons have much smaller gyroradius than the curvature radius, the electrons are unlikely to be influenced by the FLC scattering process. On the other hand, ring current ions (H^+, He^+, O^+) with comparable gyroradius can experience scattering. Among the three species, the O^+ has the largest gyroradius, so it would experience the FLC scattering most easily. In this study, we only consider the FLC effect on the ion scattering.

3 Simulation results

In order to understand the role of FLC scattering mechanism in ion precipitation and the decay of ring current intensity, we perform two simulations with the FLC scattering process included and excluded, respectively. The storm event is chosen at March 17, 2013, a CME-driven event with its minimum Dst approaching -140 nT. Figure 1 shows the solar wind, interplanetary, and geomagnetic conditions. The largely increased solar wind speed, solar wind density, and southward turning of the IMF Bz component lead to the enhancement of Dst and AE index, corresponding to the sudden storm commencement (SSC). For the rest of the day, substantial substorm injections continue and the Dst index decreases to -100 nT around 10:30 UT and further drops to around -140 nT at 20:00 UT, after which the recovery phase begins.

3.1 Morphology of ion precipitation associated with FLC scattering

Figure 2 shows the global distribution of the rigidity parameter ε and the corresponding pitch angle diffusion coefficients $D_{\alpha\alpha}$ for different ion species at E=50 keV and α= 50°. All these plots are chosen at the time of the first Dst minimum (i.e., 10:30 UT). The ε value for all ion species is generally larger on the nightside than on the dayside, a result of that the nightside magnetic field lines are more stretched with smaller field line curvature. As the O^+ ion has the largest gyroradius among the three, its ε is the greatest, and it would experience the FLC scattering on the dayside the most easily since it meets the criterion of $\varepsilon > 0.1$ in a wider region than He^+, and even much wider than H^+. As expected, the pitch angle diffusion coefficient $D_{\alpha\alpha}$ above the FLC scattering threshold, i.e., the non-blank area in the plot (middle column), shows wider coverage over the globe, although the magnitude is not necessarily the largest. Figure 2 (right column) shows that in general, for individual ion species, the $D_{\alpha\alpha}$ is larger at higher energies, and reaches the highest around the pitch angle of 50°, suggesting that the FLC mechanism can more effectively scatter ions with higher energies and intermediate pitch angles. Among the three ions, the diffusion coefficient for the H^+ appears to be the largest for higher energies (E>10 keV), but it is smaller at lower energies (E<10 keV). The coefficient of O^+ is larger at lower energies. Such a reversed order in the $D_{\alpha\alpha}$ indicates that for ions at a particular kinetic energy E and pitch angle, the scattering efficiency is larger for O^+ ions when E is small, but it is larger for H^+ ions when E is larger.

Figure 3 compares the total precipitating flux within the ion loss cone at different energies from two simulations at 10:30 UT. The results without FLC scattering loss show that precipitation mostly occurs on the dusk-to-nightside sector outside L of 3.5. Ions with lower energies are precipitated more. The H^+ ions show the largest precipitating flux among the three species and He^+ ions precipitate the least. Such precipitation is a result of magnetospheric convection; as the particles are transported earthward and the loss cone widens, particles with small pitch angles precipitate [*Jordanova et al.*, 1996]. Regardless of the ion species and the intensity of the flux, the global morphology of the precipitation is the same for these ions. That is, the precipitation occurs in the same MLT region outside the plasmapause for the same energy.

As the FLC scattering is included in the simulation, the precipitation on the nightside increases significantly. Among the three ion species, the H^+ and He^+ precipitation mostly takes place in the outer region (L>5) in the nightside sector, while the O^+ precipitation zone extends into the afternoon and morning sectors, in addition to the nightside region. Its radial coverage is also much larger on the nightside. Ions with higher energies tend to precipitate slightly in the inner region and more into the dayside sector. In contrary to the H^+ precipitation, the O^+ precipitation at E = 50 keV shows asymmetry in the global pattern. The precipitation is much less on the dawn-to-noon sector than the other area, possibly an indication on the drift path of source population as they move around the Earth.

From the global distribution of proton precipitation with the FLC scattering included, we can easily identify the sharp earthward boundary of the precipitation for these ions, which may be related to the isotropy boundary. It is evident that the precipitation boundary is not only energy and MLT dependent but also ion species dependent. For example, the boundary of E=50 keV H^+ is around L = 5 at the midnight and moves outwards to L = 6 on the dawnside/duskside. In other words, the ionospheric latitude for the precipitation boundary is at the lowest latitudes on the midnight and shifts to higher latitudes while moving eastward or westward. Such boundary is further earthward at higher energies. In contrast, the precipitating boundary of O^+ is even closer to the Earth then the light ions. These tendencies were also reported in previous studies [e.g., *Yue et al.*, 2014] that estimated the isotropy boundary based on the criterion of $K = 8$ (or $\varepsilon = 0.125$). Thus, the FLC scattering may be associated with the formation of isotropy boundary, as will be discussed below.

3.2 Contribution of FLC scattering to the ring current decay and ionospheric precipitation

As shown above, the FLC scattering brings about substantial ion precipitation compared to the adiabatic loss by magnetospheric convection, meaning that the ring current loses a large amount of ion population. Figure 4 shows the simulated Dst index compared to the observed SYM-H index. The simulation uses Dessler-Parker-Sckopke (DPS) relationship [*Dessler and Parker*, 1959; *Sckopke*, 1966] to estimate the energy content of the ring current and then determine the associated Dst index.

The ring current between 06:00 and 10:00 UT drops rapidly in both simulations, suggesting that the energization process dominates over the loss processes in the storm main phase. On the other hand, the ring current is remarkably weaker in the recovery phase when the FLC effect is considered and recovers slightly faster than the case without the FLC scattering. The difference between the two Dst indices is about 15 nT, a factor of 20%, implying that the FLC scattering of ions additionally removes about 20% of the ion population from the ring current populations. It should be noted that the ring current model only simulates the ring current while the observed SYM-H index represents the contribution from all types of current systems, including the magnetopause current and tail currents, which are absent in the model. This is probably the reason that the overall Dst index in the simulation is not as strong as in the observation.

We further compare the precipitation with in-situ measurements from low-earth orbit (LEO) NOAA/POES satellites. With several identical spacecraft flying along different meridians, global coverage of precipitation is obtained. Figure 5 (a) shows observed proton precipitation of 30<E<80 keV at four MLT sectors. The data is binned every 0.5 hour with a radial resolution of 0.25 R_e. The proton precipitation on the dusk-to-night sector (15<MLT<3) is profound during the storm main phase as well as in the prolong recovery phase. In the storm main phase from 06:00 to 10:30 UT, the inner region with 3.5<L<5 is gradually filled up with loss cone protons. In the recovery phase, the earthward inner boundary of precipitation slightly migrates outwards with the precipitation intensity decreased. In the sector of 15<MLT<21, the outer region (L>5) shows nearly lack of precipitation after 18:00 UT, while the inner region still possesses strong precipitating flux. On the morning and dayside (3<MLT<15), the precipitation mostly occurs outside L=4.5, and is much weaker in both the storm main phase and recovery phase.

In the simulation without FLC scattering, the proton precipitation (30-80 keV) in the dusk-to-night sector (15<MLT<3) appears within a large region outside L=3 in the storm main phase and recovery phase, similar to the distribution in observations. However, the magnitude is notably smaller, suggesting that the loss of protons from magnetospheric convection at 30<E<80 keV in the model cannot account for the observed precipitation. When the FLC scattering loss is introduced, it is found that the proton precipitation in the outer zone (L>5.5) is largely enhanced, which therefore

agrees better with the observation qualitatively. In the midnight sector (21<MLT<3), the intensity appears larger than the data in the same zone. In the dusk sector (15<MLT<21), the outer zone precipitation is weaker and remarkably drops after 18:00 UT, which is consistent with the data. However, across all the MLTs, the inner region (3.5<L<5) still lacks sufficient precipitation, which may be attributed to the missing of other necessary collisionless loss mechanisms, such as EMIC waves.

Similarly, with the FLC scattering loss included, the O^+ precipitation is significantly enhanced in the outer zone (L>4.5 on the nightside, and L>5 on the dayside), as opposed to the case without FLC scattering loss, in which only weak precipitation occurs in the dusk and night sectors and it is completely empty on the dayside. The O^+ precipitation appears across a wider L region than the proton precipitation, although the precipitation intensity for 30<E<80 keV is not as large. It further shows larger flux on the dayside (9<MLT<15) that is missing in the proton precipitation (Since no O^+ precipitation is available from the POES satellite, comparisons are not made available).

3.3 Energy source to the ionosphere due to ion precipitation

We further investigate the contribution of the ion precipitation to the ionospheric energy deposit by comparing with the electron precipitation. It is widely believed that the electron precipitation contains the dominant energy source into the upper atmosphere and the contribution of ions is usually omitted. With the FLC scattering process included, we compare the consequent contribution from all ion species. Figure 6 shows the spatial distribution of precipitating energy flux of electrons, protons, helium ions, and oxygen ions at 10:30 UT. The precipitating energy flux is computed by integrating the differential flux within the loss cone over 150 eV<E<400 keV. The electron precipitation clearly dominates the energy budget from the post-midnight eastward to the dayside. On the nightside, large electron precipitation extends to latitudes as low as 51° and the energy deposit almost reaches 10 $ergs/cm^2/s$ at MLT=9 and MLat = 60°. In contrast, the ion precipitation is mostly centered around the midnight and decreases towards dayside. The proton energy flux is the largest among the three ion populations, followed by the oxygen and helium ions. It is noted that on the nightside (21<MLT<3), the proton energy flux appears to be close to that of electrons

at mid-latitudes, suggesting that the proton precipitation also carries considerable energy source down to the upper atmosphere on the nightside.

Figure 7 shows the temporal evolution of precipitating energy flux at midnight (MLT=24). The energy flux of each species is significantly enhanced after 06:00 UT as the storm begins and the nightside magnetic field stretches. While increased electron precipitating energy flux frequently penetrates to lower latitudes, possibly by enhanced wave-particle interactions as tail plasma are injected earthward, the ions mostly contribute to latitudes above 55°, where the magnetosphere undergoes large stretching. The intensity of the energy flux due to proton precipitation is close to that of electrons throughout the storm main phase, indicating that on the nightside, ion precipitation owing to the FLC scattering also produces remarkable energy source to the ionosphere, which may further enhance the ionization in the upper atmosphere and local conductivity. In our next study, we will incorporate this additional energy source in the calculation of the ionospheric conductance. Again, the oxygen ions provide a larger coverage of precipitation source energy, but at a secondary level in its intensity as compared to protons.

3.4 Relationship with the isotropy boundary

Finally, whether the FLC scattering is associated with the formation of isotropic boundary is examined. We follow the methods in *Dubyagin et al.* [2018] to identify the IB location from NOAA satellite observations of 30-80 keV proton fluxes. Two NOAA satellites (MetOP-02 and NOAA-19) travel through the auroral zone in the pre-midnight and post-midnight sector respectively during the storm event, and thus provide a good opportunity to compare with simulation results because the FLC scattering process is predominantly effective on the nightside. As demonstrated in Figure 8 (a, b), across the boundary towards lower latitudes (or lower L shells), the precipitating (from 0° telescope) proton flux is lower than the trapped (from 90° telescope) proton flux and deviates more and more as moving towards equatorward (lower L shells). The two are however in comparable magnitude at higher latitudes (larger L shells) of the boundary (i.e., a signature of isotropic distribution). In case of encountering two boundaries (high-latitude and low-latitude IBs) [*Dubyagin et al.*, 2018], we choose the high-latitude boundary because the low-latitude boundary may be attributed to local dynamics such as EMIC waves.

Figure 8 (c) shows IB locations (solid lines) obtained from the two satellites. During the entire storm event, although their orbits slightly shift in local times, the variation is small within 1-2 local hours. From the simulation results, we obtain the boundary along the satellite trajectory by selecting the position where the rigidity parameter of $\varepsilon = 0.1$ for protons of 50 keV, a criterion used in many previous studies [e.g. *Serggev et al.*, 1983; *Ganushkina et al.*, 2005; *Yue et al.*, 2014]. It is found that in storm time, the boundary determined from the model results move to lower L shells, consistent with the trends in the data, although at pre-storm time, the model shows a much more earthward location than the data. During the storm time (after 09:00 UT), the model's boundary is around 4.5, while the observations show that IB locations generally fluctuate between L=3.5 and L=4.5, slightly closer to the Earth than the model results. Hence, the modeled isotropic boundary is at larger L-shells than observations by about 20%, indicating that the stretching of the nightside magnetic field lines and subsequent FLC scattering is roughly responsible for the formation of sharp IB boundaries.

4 Summary

In this study, we implement an additional collisionless loss mechanism in the ring current model: field line curvature (FLC) scattering, and investigate its effects on the ring current decay and contribution to the ionospheric energy source and auroral isotropic boundary. The FLC scattering mechanism is solved via a diffusion equation with associated pitch angle diffusion coefficients. Ions with comparable gyroradius to the field line curvature radius undergo scattering and further precipitate down to the ionosphere when they are in the loss cones. The results are summarized as follows.

1. The FLC scattering mechanism can effectively diffuse ring current ions on the nightside where the magnetic field lines are more stretched. Compared to the protons, the heavy oxygen ions experience the scattering over a wider region due to its larger gyroradius. The precipitation of protons takes place mainly on the nightside outside L=5, while the oxygen ions precipitate outside L=4 and even on the dayside. With the FLC scattering included, the ring current energy content decreases and recovers sooner.

2. The comparisons with NOAA/POES 30-80 keV proton precipitating flux demonstrate that the FLC scattering could account for the precipitation in the outer zone (L>5) on the nightside. But more precipitating flux is needed in the inner zone down to L=3.5. Such additional scattering process can be due to the EMIC waves, which is being investigated in an ongoing project in our team.
3. The precipitating proton energy flux can at times be comparable to that of electrons at midnight, suggesting that the ion precipitation also contributes significantly to the ionospheric energy deposit and cannot be neglected. The oxygen ion precipitation, although at a smaller intensity, occurs with a larger coverage at mid-latitudes. These additional energy source into the ionosphere will be considered in our next study for a more comprehensive calculation of ionospheric conductance.
4. The isotropic boundary, determined from NOAA satellites that travel across the pre-midnight and post-midnight sectors, is compared to the FLC-associated boundary (i.e., $\varepsilon = 0.1$, below which no scattering takes places and isotropic precipitation sharply drops). General agreement of the two locations is achieved, although a small discrepancy of about 20% exists. The model's boundary where isotropic precipitation sharply drops during storm time is around L=4.5, while the observations show the isotropic boundary between 3.5-4.5. We can therefore conclude that the FLC scattering process could explain the formation of isotropic boundary to a large extent.

Acknowledgments

The authors thank the OMNIweb from NASA Goddard Space Flight Center for providing the solar wind/interplanetary data and the Kyoto, Japan World Data Center System for providing the SYM-H index and AE-index. The authors are also grateful to NOAA website for providing POES data (http://satdat.ngdc.noaa.gov/sem/poes/). The RAM-SCB model code is available at https://github.com/lanl/RAM-SCB.

The simulation data is available at https://doi.org/10.5281/zenodo.3631152 [*Yu et al.*, 2020]. Simulations were performed on TianHe-2 at National Supercomputer Center in Guangzhou, China. The work at Beihang University was supported by the NSFC grants 41574156, 41821003, and 41974192.

The work at Los Alamos was conducted under the auspices of the U. S. Department of Energy, with partial support from the National Aeronautics and Space Administration.

References

Albert, J. M. (2005), Evaluation of quasi-linear diffusion coefficients for whistler mode waves in a plasma with arbitrary density ratio, *Journal of Geophysical Research: Space Physics*, *110*(A3), doi:10.1029/2004JA010844, a03218.

Chen, L., V. K. Jordanova, M. Spasojevic, R. M. Thorne, and R. B. Horne (2014), Electromagnetic ion cyclotron wave modeling during the geospace environment modeling challenge event, *Journal of Geophysical Research Space Physics*, *119*(4), 2963–2977.

Chen, M. W., C. L. Lemon, J. Hecht, S. Sazykin, R. A. Wolf, A. Boyd, and P. Valek (2019), Diffuse auroral electron and ion precipitation effects on rcm-e comparisons with satellite data during the 17 march 2013 storm, *Journal of Geophysical Research: Space Physics*, *0*(0), doi: 10.1029/2019JA026545.

Delcourt, D. C., J. A. Sauvaud, R. F. M. Jr, and T. E. Moore (1996), On the nonadiabatic precipitation of ions from the near-earth plasma sheet, *Journal of Geophysical Research Space Physics*, *101*(A8), 17,409–17,418.

Dessler, A. J., and E. N. Parker (1959), Hydromagnetic Theory of Geomagnetic Storms, *J. Geophys. Res.*, *64*, 2239–2252, doi:10.1029/JZ064i012p02239.

Dubyagin, S., N. Y. Ganushkina, and V. Sergeev (2018), Formation of 30kev proton isotropic boundaries during geomagnetic storms, *Journal of Geophysical Research: Space Physics*, *123*(5), 3436–3459, doi:10.1002/2017JA024587.

Ebihara, Y., M.-C. Fok, T. J. Immel, and P. C. Brandt (2011), Rapid decay of storm time ring current due to pitch angle scattering in curved field line, *Journal of Geophysical Research: Space Physics*, *116*(A3), doi:10.1029/2010JA016000.

Fernandes, P. A., B. A. Larsen, M. F. Thomsen, R. M. Skoug, G. D. Reeves, M. H. Denton, R. H. W. Friedel, H. O. Funsten, J. Goldstein, M. G. Henderson, J.-M. Jahn, E. A. MacDonald, and D. K. Olson (2017), The plasma environment inside geostationary orbit: A van allen probes hope survey, *Journal of Geophysical Research: Space Physics*, *122*(9), 9207–9227, doi:10.1002/2017JA024160.

Frey, H. U. (2007), Localized aurora beyond the auroral oval, *Reviews of Geophysics*, *45*(1).

Fuselier, S. A., S. P. Gary, M. F. Thomsen, E. S. Claflin, B. Hubert, B. R. Sandel, and T. Immel (2004), Generation of transient dayside subauroral proton precipitation, *Journal of Geophysical Research: Space Physics*, *109*(A12), doi:10.1029/2004JA010393.

Ganushkina, N. Y., T. I. Pulkkinen, M. V. Kubyshkina, V. A. Sergeev, E. A. Lvova, T. A. Yahnina, A. G. Yahnin, and T. Fritz (2005), Proton isotropy boundaries as measured on mid- and low-altitude satellites, *Annales Geophysicae*, *23*(5), 1839–1847, doi:10.5194/angeo-23-1839-2005.

Gilson, M. L., J. Raeder, E. Donovan, Y. S. Ge, and L. Kepko (2012), Global simulation of proton precipitation due to field line curvature during substorms, *Journal of Geophysical Research: Space Physics*, *117*(A5), doi:10.1029/2012JA017562.

Glauert, S. A., and R. B. Horne (2005), Calculation of pitch angle and energy diffusion coefficients with the PADIE code, *Journal of Geophysical Research (Space Physics)*, *110*, A04206, doi:10.1029/2004JA010851.

Glauert, S. A., R. B. Horne, and N. P. Meredith (2014), Three-dimensional electron radiation belt simulations using the BAS Radiation Belt Model with new diffusion models for chorus, plasmaspheric hiss, and lightning-generated whistlers, *Journal of Geophysical Research (Space Physics)*, *119*, 268–289, doi:10.1002/2013JA019281.

Haiducek, J. D., N. Y. Ganushkina, S. Dubyagin, and D. T. Welling (2018), On the accuracy of adiabaticity parameter estimations using magnetospheric models, *Journal of Geophysical Research: Space Physics*, *124*(3), 1785–1805, doi:10.1029/2018JA025916.

Horne, R. B., T. Kersten, S. A. Glauert, N. P. Meredith, D. Boscher, A. Sicard-Piet, R. M. Thorne, and W. Li (2013), A new diffusion matrix for whistler mode chorus waves, *Journal of Geophysical Research (Space Physics)*, *118*, 6302–6318, doi:10.1002/jgra.50594.

Hubert, B., J. C. Grard, S. A. Fuselier, and S. B. Mende (2003), Observation of dayside subauroral proton flashes with image-fuv., *Geophysical Research Letters*, *30*(3), 263–263.

Ilie, R., N. Ganushkina, G. Toth, S. Dubyagin, and M. W. Liemohn (2015), Testing the magnetotail configuration based on observations of low-altitude isotropic boundaries during quiet times, *Journal of Geophysical Research: Space Physics*, *120*(12), 10,557–10,573, doi:10.1002/2015JA021858.

Immel, T. J., S. B. Mende, H. U. Frey, L. M. Peticolas, C. W. Carlson, J. C. Gerard, B. Hubert, and S. A. Fuselier (2002), Precipitation of auroral protons in detached arcs, *Geophysical Research Letters*, *29*(11), 14–114–4.

Jordanova, V. K., L. M. Kistler, J. U. Kozyra, G. V. Khazanov, and A. F. Nagy (1996), Collisional losses of ring current ions, *Journal of Geophysical Research Space Physics*, *101*(A1), 111.

Jordanova, V. K., J. U. Kozyra, A. F. Nagy, and G. V. Khazanov (1997), Kinetic model of the ring current-atmosphere interactions, *Journal of Geophysical Research (Space Physics)*, *102*, 14,279–14,292, doi:10.1029/96JA03699.

Jordanova, V. K., Y. S. Miyoshi, S. Zaharia, M. F. Thomsen, G. D. Reeves, D. S. Evans, C. G. Mouikis, and J. F. Fennell (2006), Kinetic simulations of ring current evolution during the Geospace Environment Modeling challenge events, *Journal of Geophysical Research (Space Physics)*, *111*, A11S10, doi:10.1029/2006JA011644.

Jordanova, V. K., M. Spasojevic, and M. F. Thomsen (2007), Modeling the electromagnetic ion cyclotron wave-induced formation of detached subauroral proton arcs, *Journal of Geophysical Research: Space Physics*, *112*(A8), doi:10.1029/2006JA012215.

Jordanova, V. K., D. T. Welling, S. G. Zaharia, L. Chen, and R. M. Thorne (2012), Modeling ring current ion and electron dynamics and plasma instabilities during a high-speed stream driven storm, *Journal of Geophysical Research (Space Physics)*, *117*(A9), doi:10.1029/2011JA017433.

Liang, J., E. Donovan, E. Spanswick, and V. Angelopoulos (2013), Multiprobe estimation of field line curvature radius in the equatorial magnetosphere and the use of proton precipitations in magnetosphere-ionosphere mapping, *Journal of Geophysical Research: Space Physics*, *118*(8), 4924–4945, doi:10.1002/jgra.50454.

Meurant, M., J.-C. Grard, C. Blockx, E. Spanswick, E. F. Donovan, B. Hubert, V. Coumans, and M. Connors (2007), El - a possible indicator to monitor the magnetic field stretching at global scale during substorm expansive phase: Statistical study, *Journal of Geophysical Research: Space Physics*, *112*(A5), doi:10.1029/2006JA012126.

Moen, J., and A. Brekke (1993), The solar flux influence on quiet time conductances in the auroral ionosphere, *grl*, *20*, 971–974, doi:10.1029/92GL02109.

Newell, P. T., V. A. Sergeev, G. R. Bikkuzina, and S. Wing (1998), Characterizing the state of the magnetosphere: Testing the ion precipitation maxima latitude (b2i) and the ion isotropy boundary, *Journal of Geophysical Research: Space Physics*, *103*(A3), 4739–4745, doi: 10.1029/97JA03622.

Ni, B., R. M. Thorne, X. Zhang, J. Bortnik, Z. Pu, L. Xie, Z.-j. Hu, D. Han, R. Shi, C. Zhou, and X. Gu (2016), Origins of the earth's diffuse auroral precipitation, *Space Science Reviews*, *200*(1), 205–259, doi:10.1007/s11214-016-0234-7.

Nishimura, Y., J. Bortnik, W. Li, L. R. Lyons, E. F. Donovan, V. Angelopoulos, and S. B. Mende (2014), Evolution of nightside subauroral proton aurora caused by transient plasma sheet flows, *Journal of Geophysical Research: Space Physics*, *119*(7), 5295–5304, doi:10.1002/2014JA020029.

Robinson, R. M., R. R. Vondrak, K. Miller, T. Dabbs, and D. Hardy (1987), On calculating ionospheric conductances from the flux and energy of precipitating electrons, *Journal of Geophysical Research (Space Physics)*, *92*, 2565–2569, doi:10.1029/JA092iA03p02565.

Sckopke, N. (1966), A General Relation between the Energ of Trapped Particles and the Disturbance Field near the Earth, *J. Geophys. Res.*, *71*, 3125–3130, doi:10.1029/JZ071i013p03125.

Sergeev, V. A., and B. B. Gvozdevsky (1995), Mt-index: a possible new index to characterize the magnetic configuration of magnetotail, *Annales Geophysicae*, *13*(10), 1093–1103, doi: 10.1007/s00585-995-1093-9.

Sergeev, V. A., M. Malkov, and K. Mursula (1993), Testing the isotropic boundary algorithm method to evaluate the magnetic field configuration in the tail, *Journal of Geophysical Research: Space Physics*, *98*(A5), 7609–7620, doi:10.1029/92JA02587.

Serggev, A. V., Sazhina, M. E., A. N., Lundblad, A. J., and Soraas (1983), Pitch-angle scattering of energetic protons in the magnetotail current sheet at the dominant source of their isotropic precipitation into the nightside ionosphere, *Planetary and Space Science*, *31*(10), 1147–1155.

Spasojevic, M., and S. A. Fuselier (2009), Temporal evolution of proton precipitation associated with the plasmaspheric plume, *Journal of Geophysical Research: Space Physics*, *114*(A12), doi: 10.1029/2009JA014530.

Spasojevic, M., H. U. Frey, M. F. Thomsen, S. A. Fuselier, S. P. Gary, B. R. Sandel, and U. S. Inan (2004), The link between a detached subauroral proton arc and a plasmaspheric plume, *Geophysical Research Letters*, *31*(4), doi:10.1029/2003GL018389.

Sraas, F., J. . Lundblad, and B. Hultqvist (1977), On the energy dependence of the ring current proton precipitation, *Planetary and Space Science*, *25*(8), 757–763.

Tsyganenko, N. A. (1982), Pitch-angle scattering of energetic particles in the current sheet of the magnetospheric tail and stationary distribution functions, *Planetary and Space Science*, *30*(5), 433–437.

Vasyliunas, V. M. (1970), Mathematical Models of Magnetospheric Convection and Its Coupling to the Ionosphere, in *Particles and Field in the Magnetosphere*, *Astrophysics and Space Science Library*, vol. 17, edited by B. M. McCormack and A. Renzini, p. 60.

Yahnin, A., and T. Yahnina (2007), Energetic proton precipitation related to ion cyclotron waves, *Journal of Atmospheric and Solar-Terrestrial Physics*, *69*(14), 1690 – 1706, doi: https://doi.org/10.1016/j.jastp.2007.02.010, pc1 Pearl Waves: Discovery, Morphology and Physics.

Yahnina, T. A., and A. G. Yahnin (2014), Proton precipitation to the equator of the isotropic boundary during the geomagnetic storm on november 20–29, 2003, *Cosmic Research*, *52*(1), 79–85, doi:10.1134/S0010952514010092.

Young, D. T., H. Balsiger, and J. Geiss (1982), Correlations of magnetospheric ion composition with geomagnetic and solar activity, *Journal of Geophysical Research: Space Physics*, *87*(A11), 9077–9096, doi:10.1029/JA087iA11p09077.

Young, S. L., R. E. Denton, B. J. Anderson, and M. K. Hudson (2002), Empirical model for scattering caused by field line curvature in a realistic magnetosphere, *Journal of Geophysical Research: Space Physics*, *107*(A6), SMP 3–1–SMP 3–9, doi:10.1029/2000JA000294.

Young, S. L., R. E. Denton, B. J. Anderson, and M. K. Hudson (2008), Magnetic field line curvature induced pitch angle diffusion in the inner magnetosphere, *Journal of Geophysical Research: Space Physics*, *113*(A3), doi:10.1029/2006JA012133.

Yu, Y., V. K. Jordanova, A. J. Ridley, G. Toth, and R. Heelis (2017), Effects of electric field methods on modeling the midlatitude ionospheric electrodynamics and inner magnetosphere dynamics, *Journal of Geophysical Research: Space Physics*, *122*(5), 5321–5338, doi:10.1002/2016JA023850, 2016JA023850.

Yu, Y., X. Tian, and V. Jordanova (2020), Ram-scb simulation outputs, doi: 10.5281/zenodo.3631152.

Yue, C., C.-P. Wang, L. Lyons, J. Liang, E. F. Donovan, S. G. Zaharia, and M. Henderson (2014), Current sheet scattering and ion isotropic boundary under 3-d empirical force-balanced magnetic field, *Journal of Geophysical Research: Space Physics*, *119*(10), 8202–8211, doi:10.1002/2014JA020172.

Yue, C., J. Bortnik, W. Li, Q. Ma, C.-P. Wang, R. M. Thorne, L. Lyons, G. D. Reeves, H. E. Spence, A. J. Gerrard, M. Gkioulidou, and D. G. Mitchell (2019), Oxygen ion dynamics in the earth's ring current: Van allen probes observations, *Journal of Geophysical Research: Space Physics*, *124*(10), 7786–7798, doi:10.1029/2019JA026801.

Zaharia, S., C. Cheng, and K. Maezawa (2004), 3-D force-balanced magnetospheric configurations, *Annales Geophysicae*, *22*, 251–265, doi:10.5194/angeo-22-251-2004.

Zaharia, S., V. K. Jordanova, M. F. Thomsen, and G. D. Reeves (2006), Self-consistent modeling of magnetic fields and plasmas in the inner magnetosphere: Application to a geomagnetic storm, *Journal of Geophysical Research (Space Physics)*, *111*, A11S14, doi:10.1029/2006JA011619.

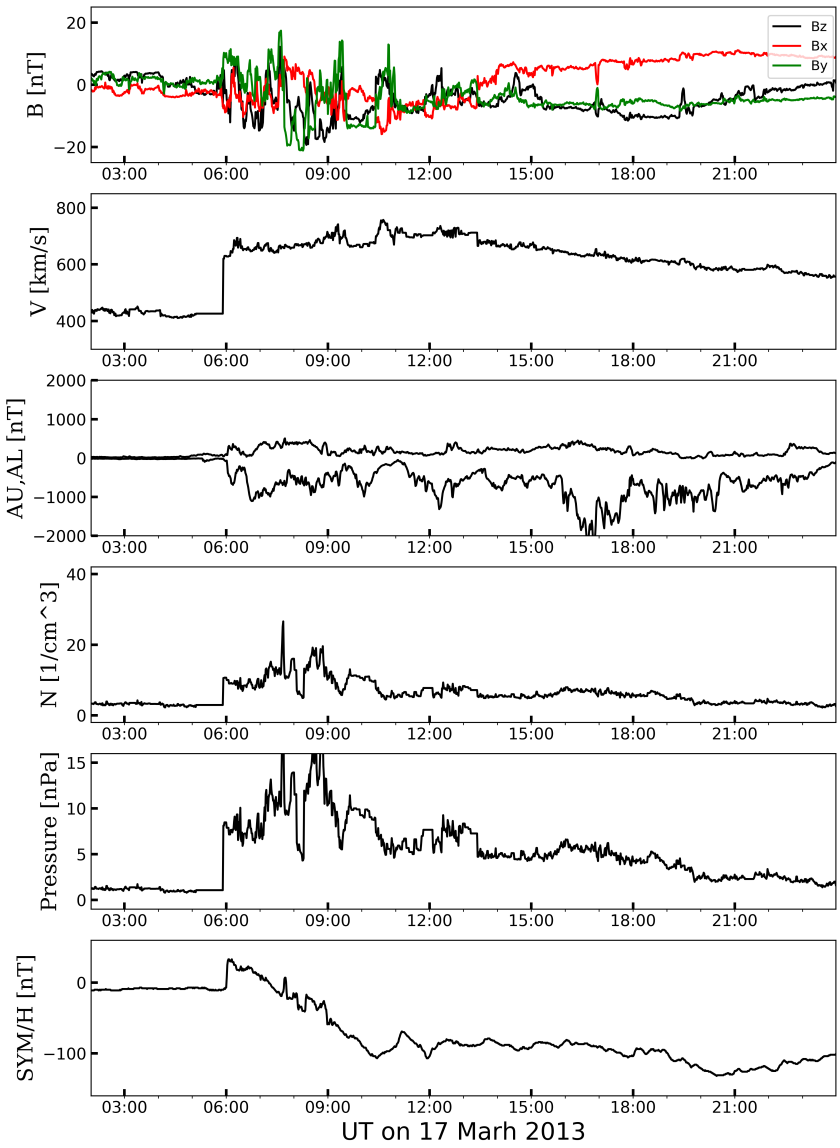

Figure 1. The solar wind, interplanetary, and geomagnetic conditions on the March 17, 2013 storm event.

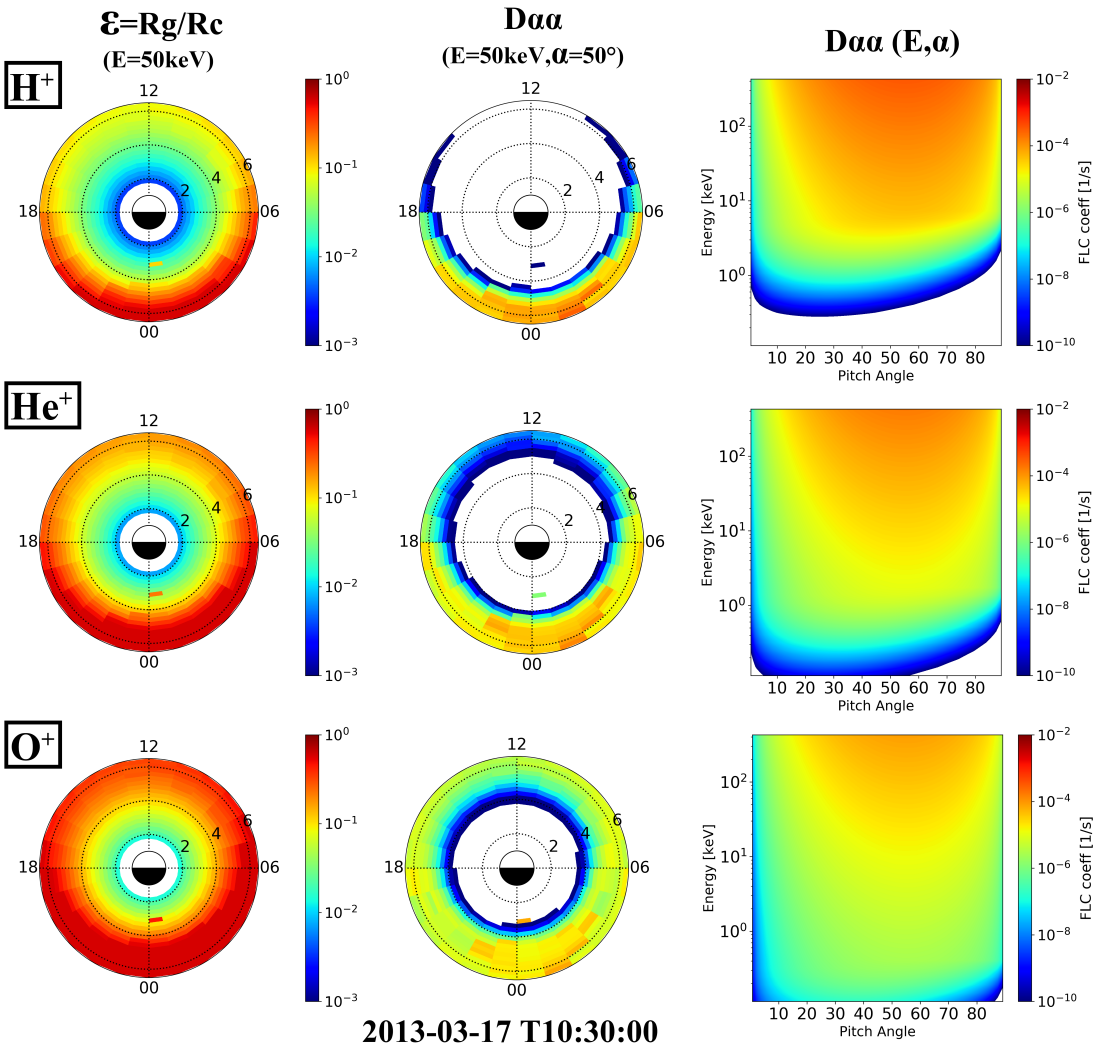

Figure 2. Left column: the rigidity parameter $\varepsilon = R_g/R_c$ for ions with E=50 keV and pitch angle of 50°. Middle column: diffusion coefficient $D_{\alpha\alpha}$ for field line scattering at E=50 keV and pitch angle of 50° in the equatorial plane. Right column: The diffusion coefficient as a function of energy and pitch angle at MLT = 24 and L=6.5. Different rows represent different ion species.

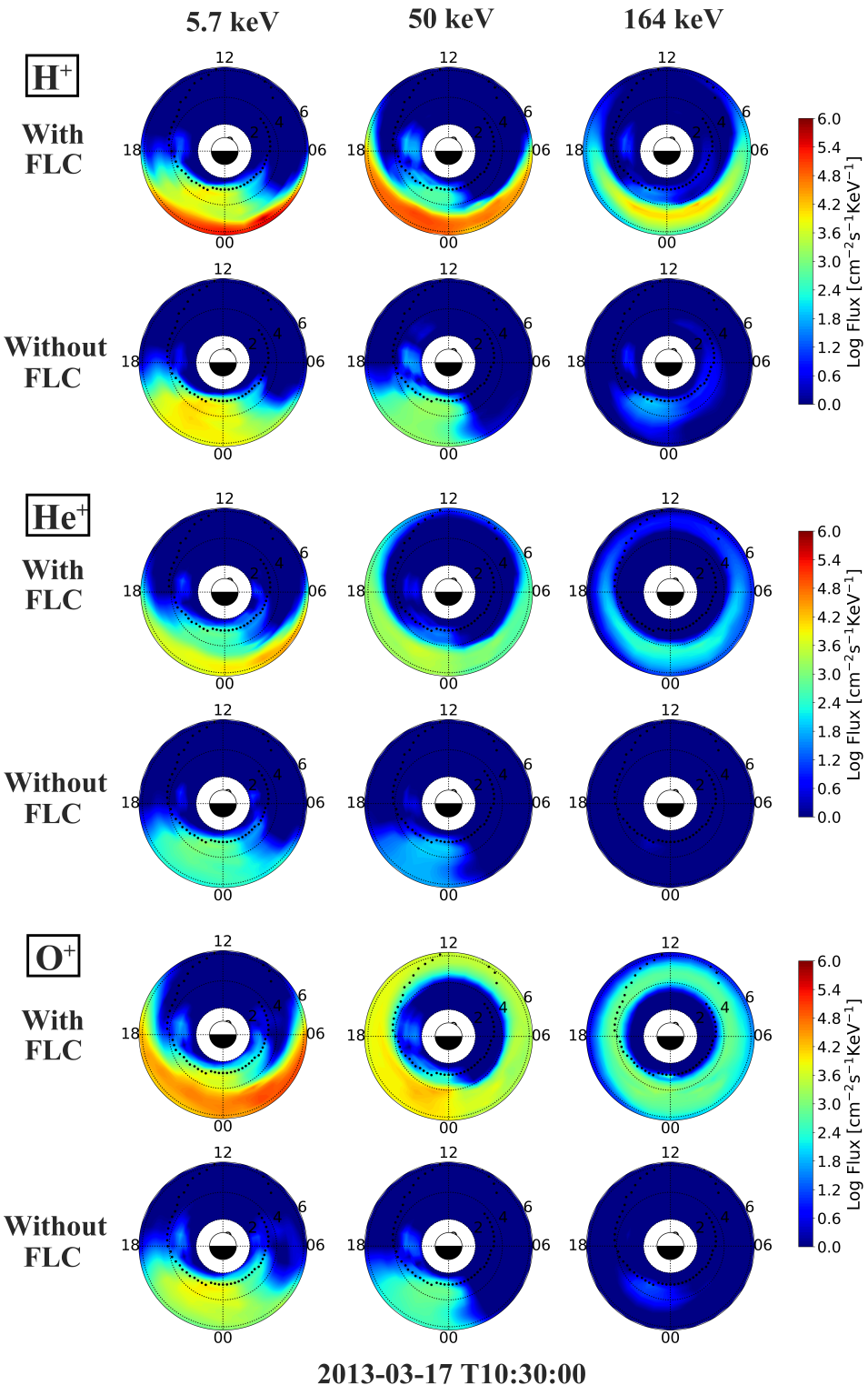

Figure 3. The global distribution of ion precipitating flux in the equatorial plane at different energies (E=5.7, 50, and 164 keV). For each ion species, the precipitation distribution is compared between two simulations: with FLC scattering included and excluded.

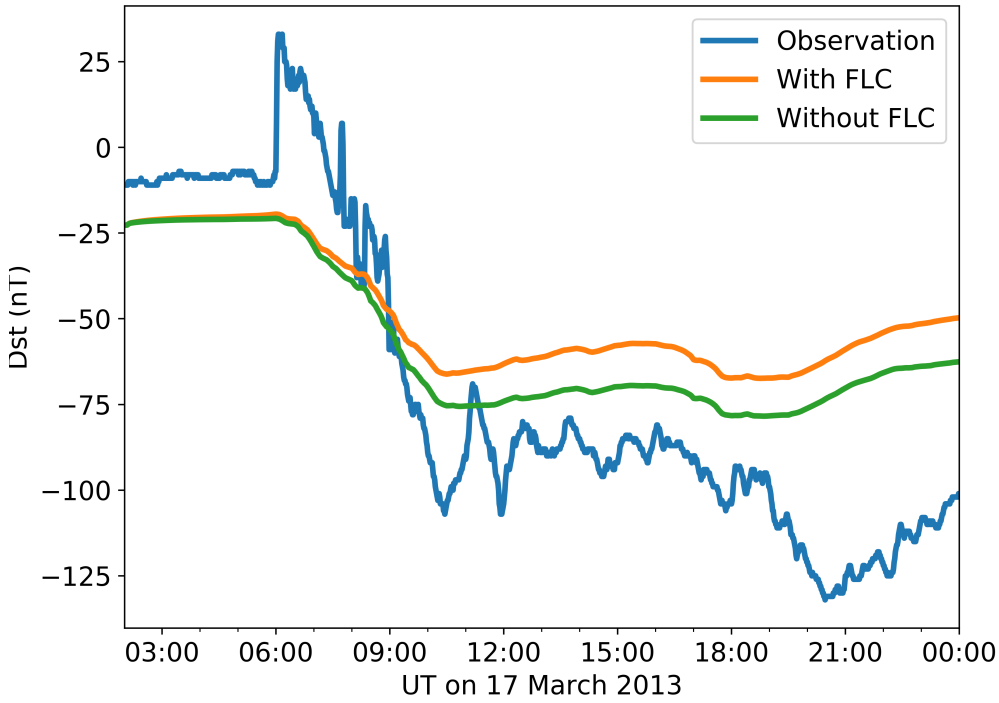

Figure 4. Dst index comparison between the observed SYM-H index and estimated index from two simulations: with the FLC scattering included and excluded.

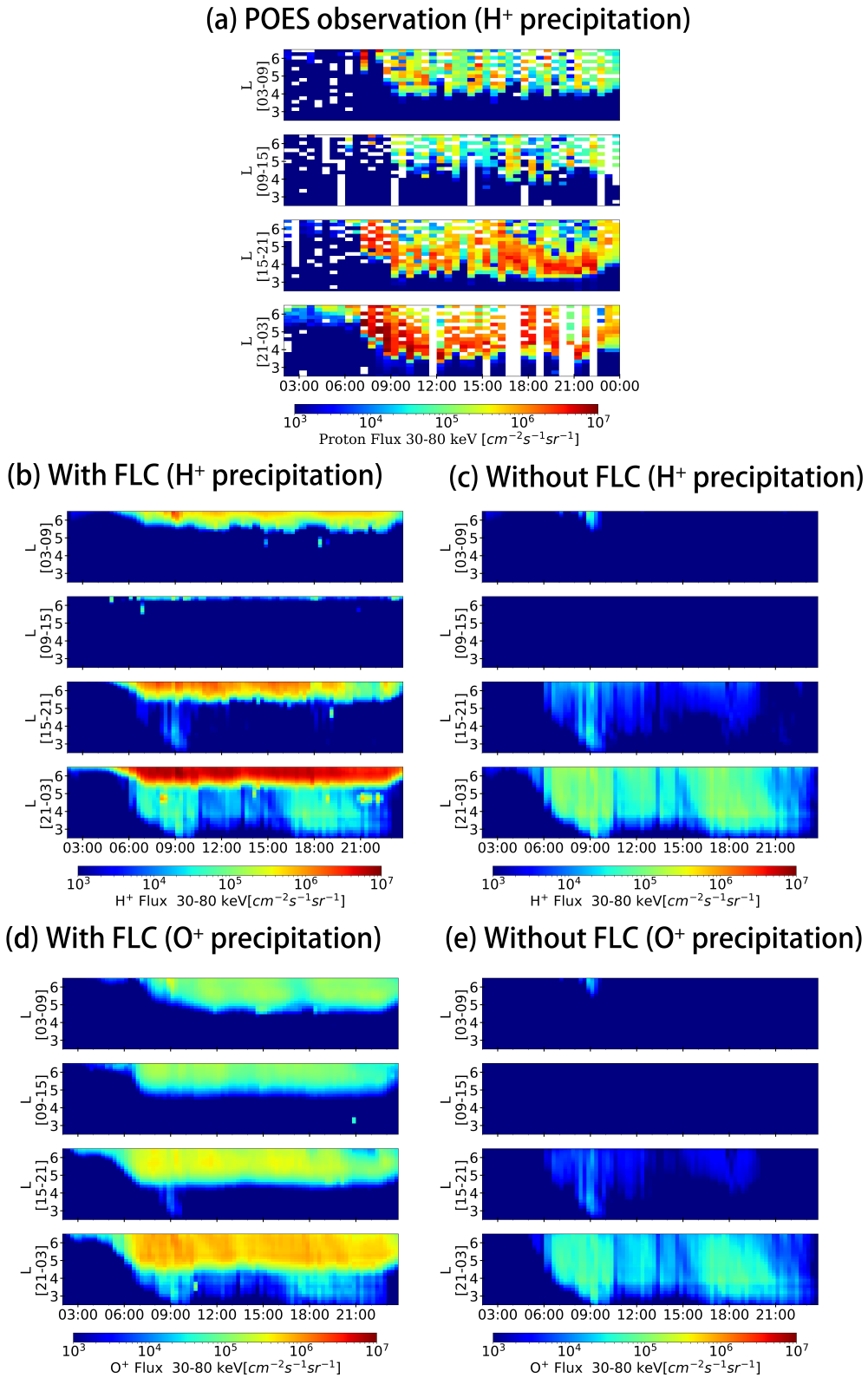

Figure 5. (a) Proton precipitating flux (30<E<80 keV) from POES observations at four different MLT sectors as a function of radial distance from the Earth and time. (b) The simulation results of proton precipitating flux with the FLC scattering included. (c) The simulation results of proton precipitating flux without the FLC scattering. (d) The simulation results of O^+ precipitating flux with the FLC scattering included. (e) The simulation results of O^+ precipitating flux without the FLC scattering.

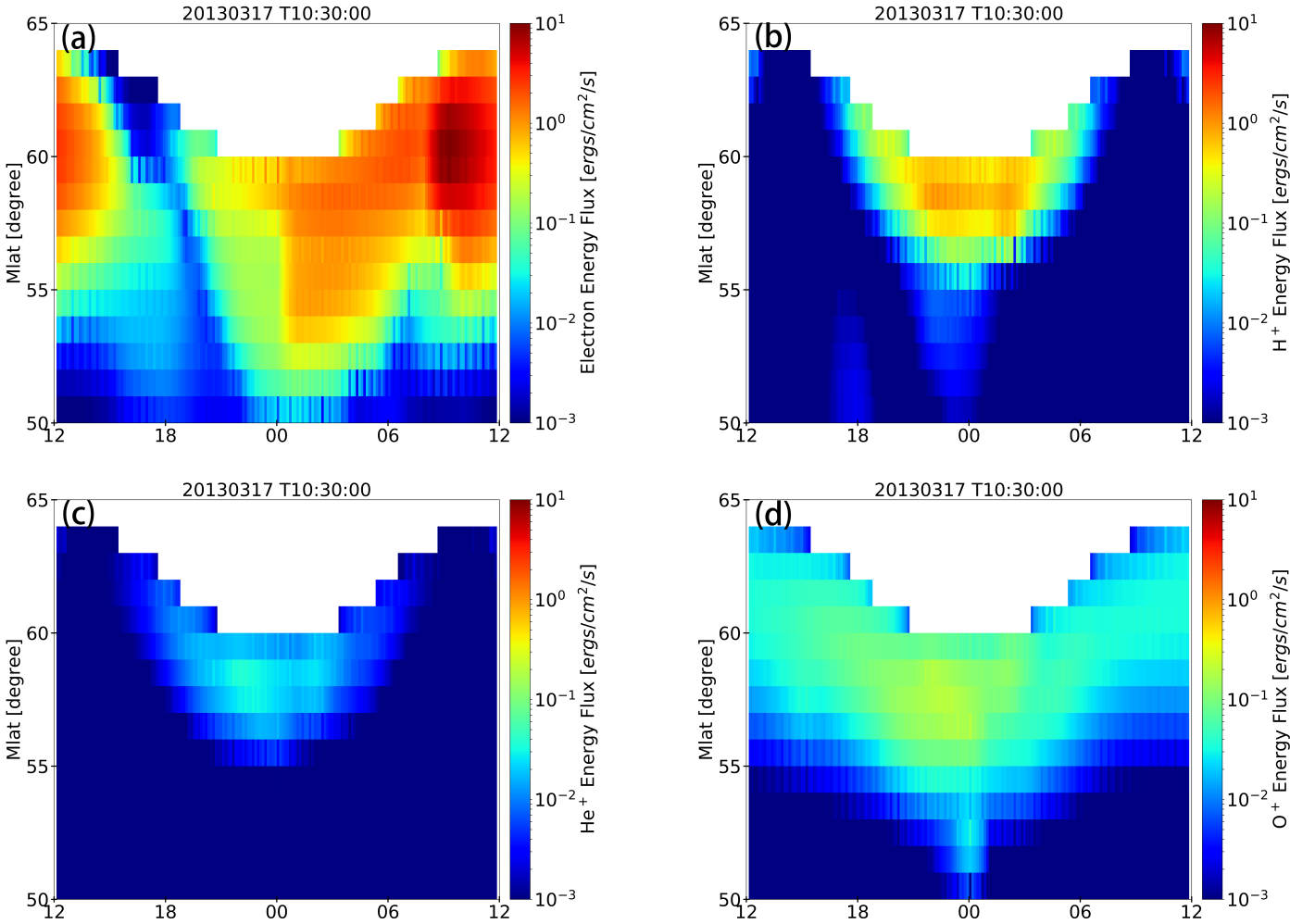

Figure 6. Spatial distribution of precipitating energy flux in the ionosphere at 10:30 UT, contributed respectively by (a) electron precipitation, (b) proton precipitation, (c) helium ion precipitation, and (d) oxygen ion precipitation. The energy flux is obtained by integrating differential flux over 150 eV<E<400 keV.

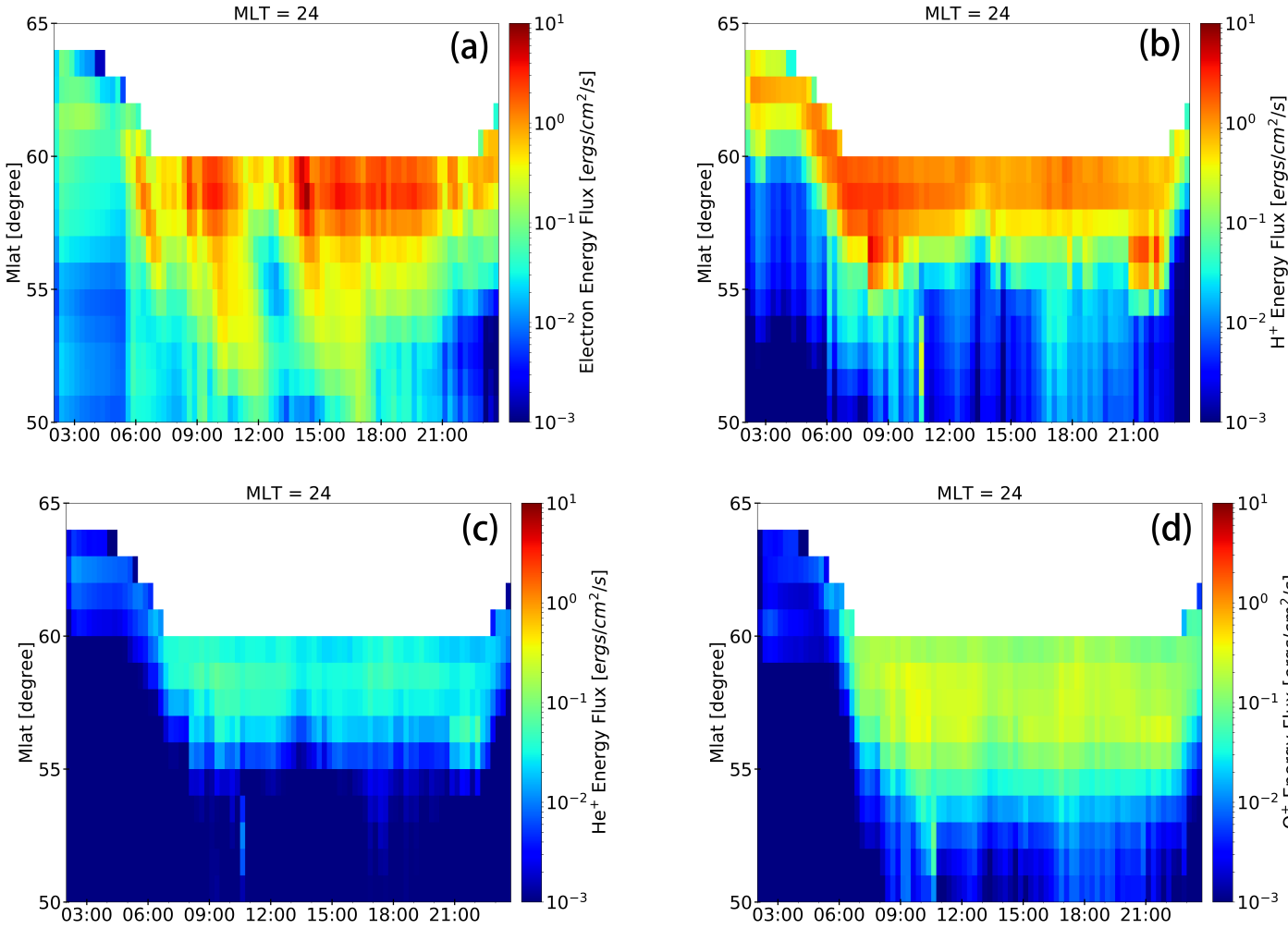

Figure 7. Temporal evolution of precipitating energy flux on the ionospheric midnight (MLT=24), contributed respectively by (a) electron precipitation, (b) proton precipitation, (c) helium ion precipitation, and (d) oxygen ion precipitation. The energy flux is obtained by integrating differential flux over 150 eV<E<400 keV.

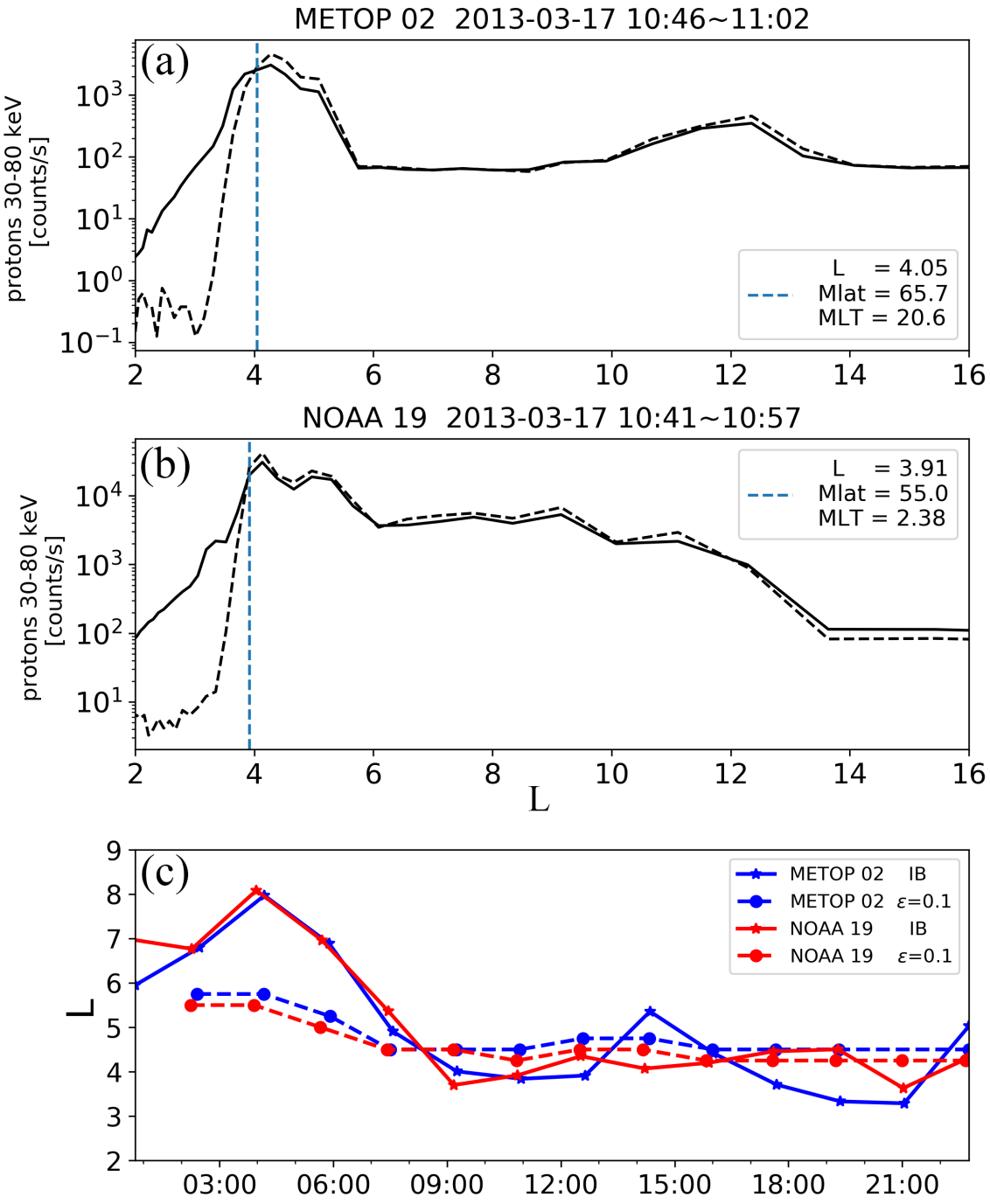

595 **Figure 8.** (a, b) Two examples of determining the isotropic boundary from Metop02 and NOAA
596 19 satellites. Dashed black line represents the precipitating proton flux observed by 0° telescope,
597 and solid black line represents the trapped proton flux observed by 90° telescope. (c) Comparisons
598 of the isotropic boundary location between the observations (solid lines) and simulations (dashed
599 lines).